Human Factors and Mechanical Engineering for Defense and Safety (2023) 7:2
https://doi.org/10.1007/s41314-023-00057-4

RESEARCH

Numerical Analysis of Thorax Injury Caused by the Blunt Impact of SIR-X Sponge Grenade

Chaoming Chen[1] · Fadong Zhao[1] · Zongmin Ma[1]

Received: 10 February 2023 / Revised: 13 February 2023 / Accepted: 10 March 2023 / Published online: 29 March 2023

Abstract
To effectively assess the injury risk of the blunt impact of the SIR-X sponge grenade on the human thorax, in this paper, we used a numerical simulation technique to test the non-lethal kinetic energy projectiles that blunt impact on the Hybrid III 50th dummy model. By simulating the effect of the L5 projectile on the thorax of the Hybrid III 50th dummy model, about NATO standard AEP-99 (2021 edition), the thoracic displacement curves of the dummy model in three testing conditions were obtained in the validation corridors. The idea of replacing the finite element model of the human body with the Hybrid III 50th dummy finite element model was proposed. We considered the difficulty in obtaining data due to the large deformation of the contact position when the SIR-X sponge grenade impacts the dummy's thorax. We proposed a mathematical model to predict the impact injury of the human thorax using the rib displacement measured by the rib displacement sensor of the Hybrid III 50th dummy. We simulated the SIR-X sponge grenade blunt impacting the dummy model's thorax. The measured rib displacement was used to predict and analyze the injury risk of the human thorax, providing a specific data reference for practical application.

Keywords Non-lethal · Kinetic energy projectiles · Injury risk · Numerical simulation

Introduction

In the assessment of blunt impact injury to the human body, blunt impact injury of the thorax should be mainly considered: first, due to the large surface area of the thorax, the probability of being impacted by the projectile is higher than that of other parts [1]; second, the thorax structure is complex, with the upper part adjacent to the head and neck and the lower part connected to the abdomen [2]. It consists of external protective structures (skin, muscles, sternum, spine, ribs, etc.) and internal soft tissue organs (heart, lungs, trachea, blood vessels, etc.). Bruising and lacerations of the skin or soft tissue may occur when a person suffers a minor impact injury to the thorax, and the ribs are compressed to the point of fracture. When the amplitude and rate of thorax compression are too large, fractures occur after ribs are squeezed beyond their tolerance limits. The internal organs pierced by broken ribs may lead to serious thorax injuries, such as pneumothorax, hemothorax, flail thorax, lung contusion, sternum fracture, heart contusion, and aortic rupture, which will be life-threatening if not treated in time [3, 4]. To reduce the possibility of serious injury, most new kinetic energy projectiles were equipped with deformable projectiles made of rubber or foam materials. The warheads absorb a certain amount of initial energy through deformation to resist impact, thus reducing the impact effect on the human thorax.

Currently, such as experimental testing and numerical simulation have been used to study blunt thorax trauma [5]. Regarding exploratory testing, impact tests were carried out with cadavers, animals, mechanical substitutes, simulation dummies, etc. to obtain biomechanical data such as force, velocity, acceleration, displacement, and stress–strain under different impact conditions and to conduct trauma grade assessment according to viscosity standard $(VC)_{max}$ [6]. Based on the analysis of current research progress, animal experiments and cadaver experiments are the most suitable for blunt ballistic impact testing [7]. However, the biomechanical response and physiological data obtained from animal experiments can only be used as a reference and cannot be directly used to predict blunt human trauma [8, 9]. The non-embalmed cadavers used in the experiments do not

✉ Chaoming Chen
275974915@qq.com

[1] Department of Equipment Management and Support, Engineering University of PAP, Xi'an, Shaanxi, China

have respiratory, cardiac cycles, muscle activity, and behavioral reflexes that are directly representative of the biological responses of living people. In addition, the cadaver sample is restricted by medical ethics, so it is difficult to obtain, and the repeatability of the experiment could be better. Even so, the corpse has achieved good injury tolerance and overall impact response results. Its experimental data can be used as baseline data to validate the impact response of alternatives [10]. The development [11, 12] of the human body finite element model with a detailed anatomical structure based on accurate geometric size has been economical, safe, and reproducible. It has eliminated the constraints of ethics, cumbersome testing procedures, expensive testing equipment, and other factors, which can provide an effective means for blunt impact injury assessment.

With the rapid development of computer technology, the use of numerical simulation as an essential tool to evaluate and better interpret the process of blunt impact has attracted wide attention [13, 14]. Therefore, we used numerical simulation technology to test the non-lethal kinetic energy projectile blunt impacting the Hybrid III 50th dummy model. This dummy model was used to predict the injury risk of B&T SIR-X sponge grenade (stated in this article SIR-X projectile) impacting the human thorax.

Modeling and Validation

Modeling of L5 Projectile

The L5 projectile is made of incompressible polyvinyl chloride (PVC) material. There are two types: long projectile and short projectile. The physical picture is shown in Fig. 1 [15], and the geometric model is shown in Fig. 2. One is 95.1 mm long, 37 mm in diameter, and 140 g in mass, while the other is 20.4 mm long, 37 mm in diameter, and 30 g in mass. The material parameters of the L5 projectile are shown in Table 1, and the grid division is shown in Fig. 3.

Regarding the modeling of the L5 projectile, it is assumed that it is a linear elastic model. Linear elastic materials are a subcategory of elastic materials, which is a good approximation for materials with small displacements, as shown by (1):

$$\sigma = f(\varepsilon) \tag{1}$$

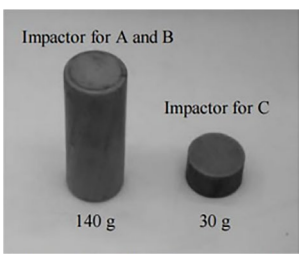

Fig. 1 Physical picture of the L5 projectiles

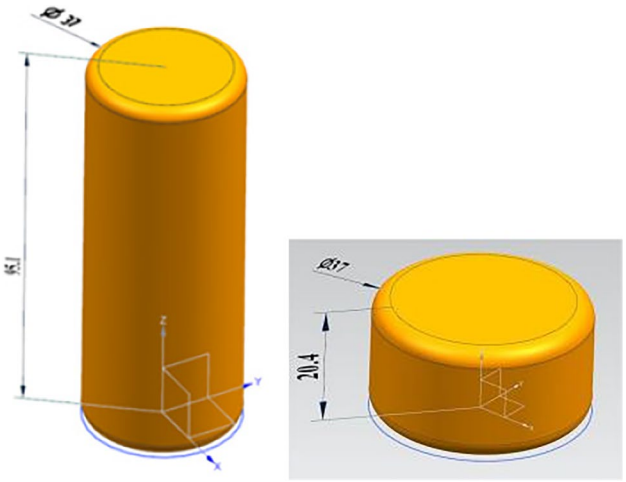

Fig. 2 Geometric model of the L5 projectiles

where σ is the stress tensor and ε is the infinitesimal strain tensor.

The stress tensor is generally divided into the spherical component (the hydrostatic stress tensor) and the deviatoric stress tensor, as shown in (2). As stress causes strain in the body, the strain tensor is also divided into normal and deviant strain tensors, both of which cause body deformation. The deformation of an object is the result of volume change caused by normal stress tensors and shape change caused by partial strain tensors. Therefore, under the load, all object element deformations correspond to the element's strain, which is superimposed with the rigid body motion. Hydrostatic stress and normal strain define the equation of state, while deviator stress and deviator strain define the strength model, as shown in Fig. 4.

An essential requirement of mechanical constitutive equations is that they should be invariant under rigid translation and rotation:

$$\sigma = pI + S \tag{2}$$

where p is the hydrostatic pressure, I is the tensor unit, and S is the deviator tensor.

$$\varepsilon = \frac{1}{3}\varepsilon_v I + \varepsilon_d \tag{3}$$

where ε is the deviator strain tensor, ε_v is the volumetric strain, I is the tensor unit, and ε_d is the deviator strain tensor.

Modeling and Validation of SIR-X Projectile

The SIR-X projectile is a fully solid hemispherical deformable projectile made of plastic cartridges and foam. We selected the SIR-X projectile as a reference in the validation process for rib cage alternatives in the NATO standard framework file AEP-99 (2021 edition) [17]. The diameter of

Table 1 Material characteristics of the L5 projectiles

	Material model	Density(kg/m^3)	Young's modulus(Gpa)	Poisson's ratio	Element type/number of elements
L5 long projectile	MAT-001 ELASTIC	1380	2.3	0.33	Hexa/30677
L5 short projectile	MAT-001 ELASTIC	1380	2.3	0.33	Hexa/10807

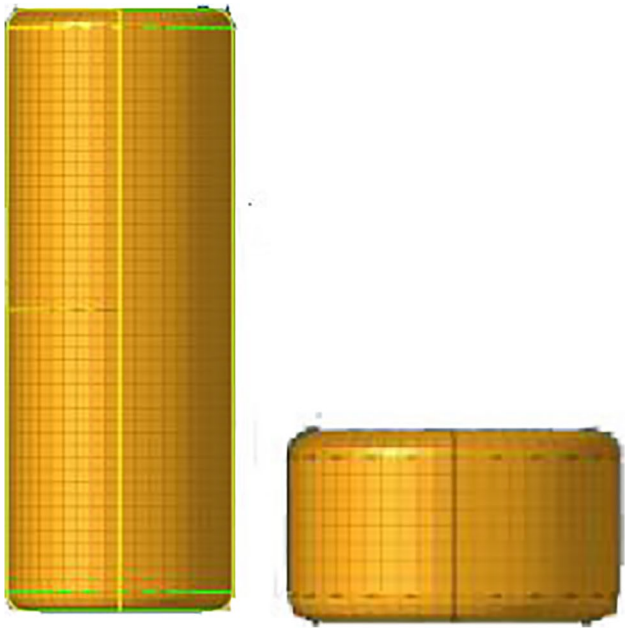

Fig. 3 Grid division diagram of the L5 projectiles

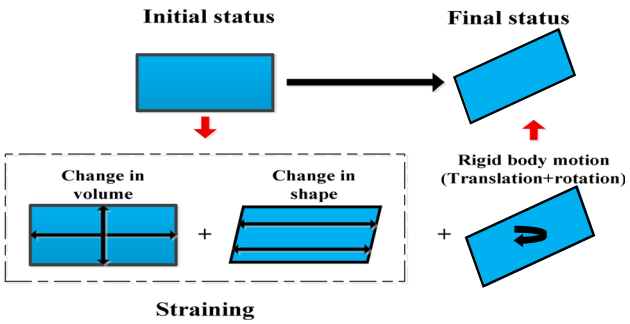

Fig. 4 Material deformation: illustration of volume and shape changes [16]

the projectile is 40 mm, and the mass is 32 g (the mass of the nose and the sabot are 7.2 g and 24.8 g, respectively). The physical picture of the projectile is shown in Fig. 5, and the geometric model is shown in Fig. 6.

Considering LS-DYNA, No. 181 simplified rubber material, and No. 1 elastic material are used to provide the nose and the sabot, respectively. The material properties are shown

Fig. 5 Physical picture of the SIR-X projectile [17]

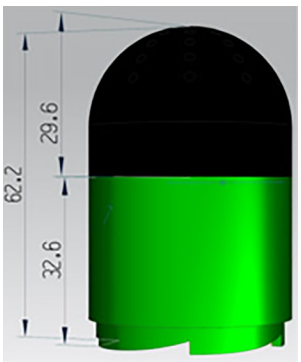

Fig. 6 Geometric model of the SIR-X projectile

in Table 2. The unloading parameters of the nose material are the hysteresis (HU) and shape (SHAPE) factors, which are used to introduce dissipation in the model (Fig. 7). To accurately obtain the dynamic compression behavior of the nose, the load model input of the nose material refers to the engineering stress–strain curve of the rigid wall impact test, as shown in Fig. 8. The junction between sabot and nose was formed into a grid by merging their respective nodes, as shown in Fig. 7.

As mentioned earlier, regarding the modeling of the SIR-X projectile, it is assumed that the sabot is a linear elastic model. The nose is considered to be a visco-hyperelastic material model. This material shows hyperelastic and viscoelastic effects. By combining the elastic component with the viscoelastic component, the viscous-superelastic component is obtained, as shown in (4):

$$\sigma = \sigma_{\text{hyperelastic}} + \sigma_{\text{viscoelastic}} \tag{4}$$

Table 2 Material characteristics of the SIR-X [20]

	Density(kg/m^3)	Bulk modulus (MPa)	Young's modulus (Gpa)	Poisson's ratio	HU	SHAPE	Element type/ number of elements
Nose	231	3000	-	0.2	0.1	15	Hexa/100160
Sabot	1354	-	23	0.387	-	-	Hexa/32140

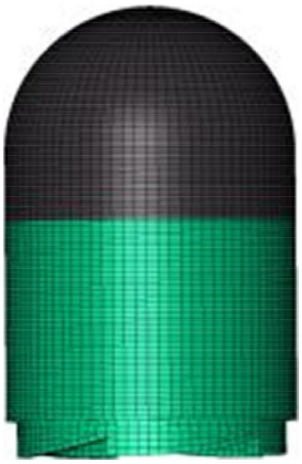

Fig. 7 Grid division diagram of the SIR-X projectile

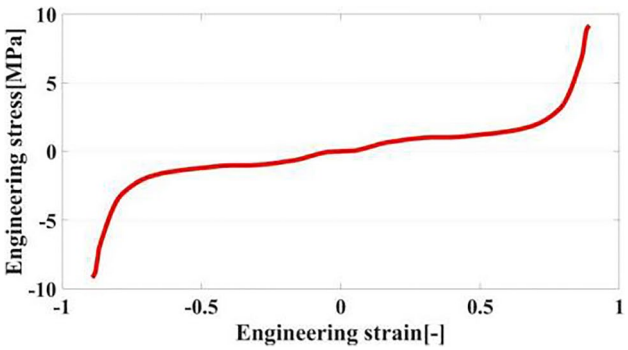

Fig. 8 SIR-X engineering stress–strain characteristics [18]

Viscoelastic Material Model

Viscoelastic materials have both fluid (viscous) and solid (elastic) properties. Considering linear materials, the constitutive equations of the linear viscoelastic material model are expressed as (5) and (6):

$$\varepsilon(t) = \int_{-\infty}^{t} J(t-s)\frac{d\sigma}{ds}ds \tag{5}$$

$$\sigma(t) = \int_{-\infty}^{t} G(t-s)\frac{d\varepsilon}{ds}ds \tag{6}$$

where $J(t)$ is the creep function, which represents the material response function under constant stress, and $G(t)$ is the stress relaxation function, which is the material response function under constant strain. Both functions are continuous concerning time. Considering (5) and (6), the response of the viscoelastic materials can be divided into two parts: viscoelastic and elastic.

Hyperelastic Material Model

Visco-hyperelastic materials are other types of elastic materials. The relationship between the load (stress) and the strain response of the material is nonlinear, and the stress emerges from the strain energy as shown in (7):

$$\sigma = \frac{\partial W}{\partial w} \tag{7}$$

where W is the strain energy density, σ is the stress tensor, and ε is the partial strain tensor. Considering the hyperelastic materials, the corresponding variable energy function must meet the frame's principle of indifference or objectivity. Therefore, (8) is derived from (7):

$$S = 2\frac{\partial W(C)}{\partial C} \tag{8}$$

where S is the second Piola–Kirchhoff stress tensor and C is the right-Cauchy strain tensor.

The SIR-X projectile is a reference projectile in NATO's standard framework files. The assessment team has defined a rigid wall-based validation method for the numerical model of the SIR-X projectile (Fig. 9). The material properties of the rigid wall are shown in Table 3. The SIR-X projectile is subjected to impact on the rigid wall (RW) at 29 m/s and 61 m/s, respectively. Moreover, whether the simulated force and displacement curves fall within the defined interval is used to validate the effectiveness of the numerical projectile model (Table 4). Figures 10 and 11 are represented snapshots of the impact loading sequences of the SIR-X projectile at specific times at two velocities.

Considering Fig. 9, T1 = 0.2 ms, the nose is no longer hemispherical owing to its straining; however, it becomes approximately cylindrical. Furthermore, T2 = 0.45 ms is chosen as the time of the onset of the densification zone. Moreover, T3 = 0.8 ms is the end of the densification regime and the end of the loading phase (the deformation of the nose reaches its maximum). Regarding Fig. 10, T1 = 0.25 ms, the

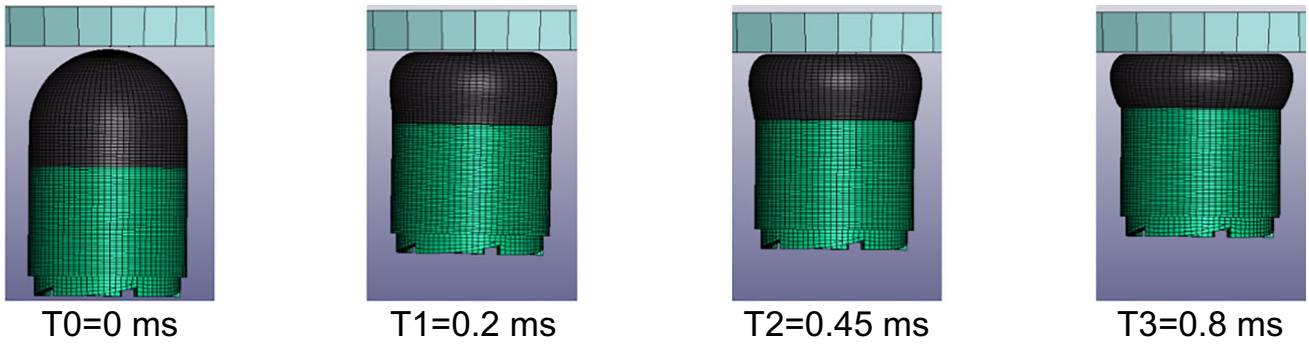

Fig. 9 Cross-section SIR-X projectile impact sequences at 29 m/s

Table 3 Material characteristics of the rigid wall

Density (kg/m^3)	Young's modulus (Gpa)	Poisson's ratio	Element type/number of elements
7890	209	0.269	Hexa/2153

nose becomes cylindrical owing to its straining. In addition, T2 = 0.37 ms is chosen as the onset of the densification zone. T3 = 0.503 ms is the end of the densification regime and the end of the loading phase (the deformation of the nose has reached its maximum). The force- and displacement–time

Table 4 Corridors for the validation of the SIR-X projectile impacting the force wall in two testing conditions

Testing conditions	Time corridor min (ms)	Displacement corridor min (mm)	Time corridor max (ms)	Displacement corridor max (mm)	Time corridor min (ms)	Force corridor min (*N*)	Time corridor min (ms)	Force corridor max (*N*)
1	0	0	0	0	0	0	0	0
	0.1	2	0.1	6	0.7	1000	0.1	1000
	0.7	16	0.6	19	0.85	1000	0.6	2300
	0.9	17	1	21	1	0	0.95	2300
	1.5	12	1.5	15	2	0	1.3	500
							2	200
2	0	0	0	0	0	0	0	0
	0.4	22	0.1	8	0.4	1000	0.1	3500
	0.47	23	0.4	26	0.45	2000	0.38	5000
	1	10	0.55	30	0.5	12,000	0.42	9000
			1	20	0.55	0	0.47	23,000
							0.62	0

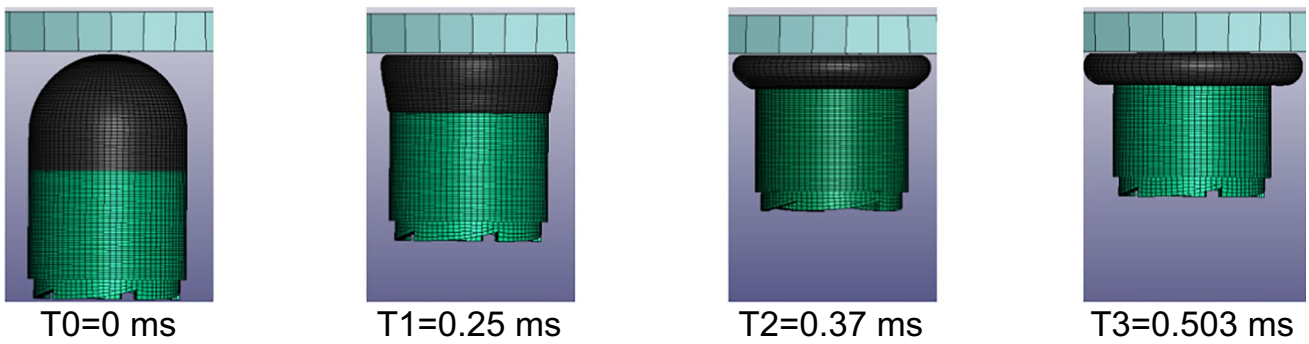

Fig. 10 Cross-section SIR-X projectile impact sequences at 61 m/s

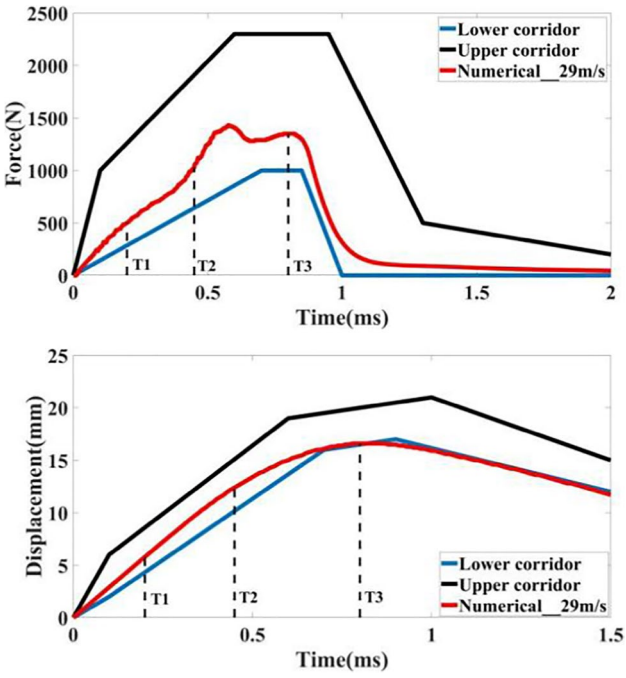

Fig. 11 Response curves of the SIR-X projectile impact on the rigid wall at 29 m/s

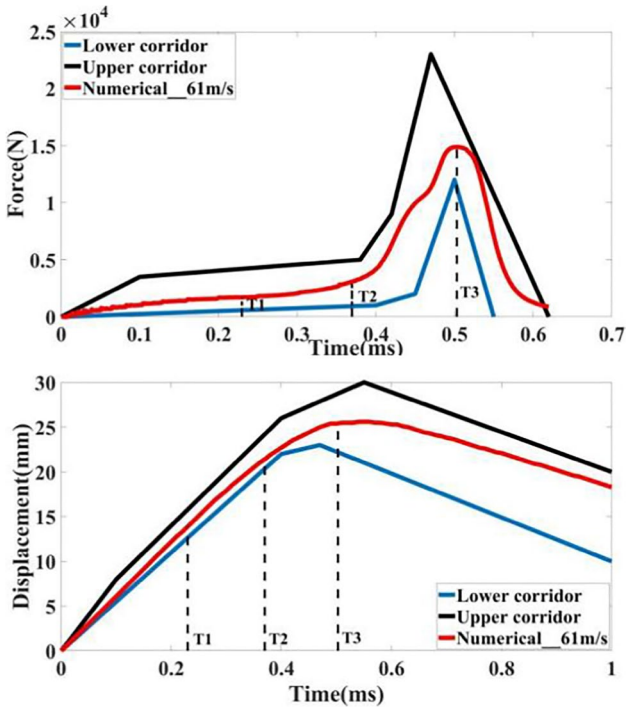

Fig. 12 Response curves of the SIR-X projectile impact on the rigid wall at 61 m/s

curves at the two velocities are shown in Fig. 9, and the time sequence of the loading phase is based on Figs. 11 and 12.

The numerical results obtained through the simulation are within the corridors defined by NATO's standard framework file AEP-99 (2021 edition), which confirms the feasibility of the constructed SIR-X projectile finite element model.

Modeling and Validation of Hybrid III 50th Dummy Model

Hybrid III 50th dummy finite element model (Fig. 13) is built with solid, shell, and beam elements in a grid size of 3–5 mm with 25,602 solid elements, 225,910 shell elements, 256 beam elements, and 276,025 nodes. The finite element model imposes perfect constraints on all parts of the dummy, and its trunk, limbs, and waist can rotate at specific angles to adapt to different collision conditions.

The thorax design of the dummy model is somewhat simplified compared with that of the human thorax. The dummy thorax model lacks organ and soft tissue filling, and the number of ribs is simplified from 12 to 6. The installed thorax plate structure plays a cushioning role in reducing direct injury to the ribs. In automobile crashes, the industry has recognized the experimental results obtained by dummies as a substitute for an occupant in automobile crash tests.

The validation of the thoracic model is given in the NATO standard AEP-99 (2021) document from WSU corridors (Table 5). Table 6 shows $(VC)_{max}$ boundary for validating the L5 projectile impacting the cadaver in three testing conditions.

Results

The impact point of L5 projectiles impacting the finite element model of the Hybrid III dummy is the middle of the third and fourth ribs of the dummy, as shown in Fig. 14.

The test results need to be filtered by CFC1000 and normalized. The digital filtering process uses ISO 648:2015, SAEJ211,

Fig. 13 Hybrid III 50th dummy model

Table 5 WSU corridors for the validation of the numerical thorax [16]

Testing conditions	Time corridor min (ms)	Displacement corridor min (mm)	Time corridor max (ms)	Displacement corridor max (mm)
5	0	0	0	0
	2	12	0.5	10
	5	18	2.3	20
			5	26
6	0	0	0	0
	2	20	1	40
	8	38	6	70
7	0	0	0	0
	1	5	0.5	12.5
	8	12	8	38

Table 6 $(VC)_{max}$ boundary for the validation of the L5 projectile impacting the cadaver in three testing conditions

Testing conditions	$(VC)_{max}$ boundary (m/s)
5	[0.24,0.51]
6	[0.65,2.35]
7	[0.14,0.6]

and other standards for reference to simulate the effects of phase-shift free filtering; phase-shift free filtering uses a four-pole Butterworth low-pass filter (CFC). According to the NATO standard AEP-99 (2021 edition) file, this section adopted the CFC 1000 filter to filter the displacement data. Normalized treatment refers to the 50th percentile male (thorax depth 236 mm) of the WSU cadaver experiment as the standard for most impact tests. Since the parts studied were concentrated on the thorax, the thorax depth of the dummy model is 273 mm, and the thorax depth scaling factor is $\lambda = 236/273 = 0.864$. The test data in three testing conditions were as follows:

Testing Condition 3

Figure 15 shows the thorax surface displacement curve and $(VC)_{max}$ curve obtained by the L5 long projectile simulating blunt impact on the dummy's thorax at 20 m/s.

Testing Condition 4

Figure 16 shows the thorax surface displacement curve and $(VC)_{max}$ curve obtained by the L5 long projectile simulating blunt impact on the dummy's thorax at 40 m/s.

Testing Condition 5

Figure 17 shows the thorax surface displacement curve and $(VC)_{max}$ curve obtained by the L5 short projectile simulating blunt impact on the dummy's thorax at 60 m/s.

From the observation of the above three figures, it can be seen that the displacement curves after filtering and normalization and $(VC)_{max}$ are within the channel specified in AEP-99 (2021 edition). We proposed that the Hybrid III dummy model can substitute for the human body model.

Discussion

Prediction of Blunt Impact Injury to the Human Thorax

We were considering the difficulty in obtaining data due to the large deformation of the contact position of the SIR-X

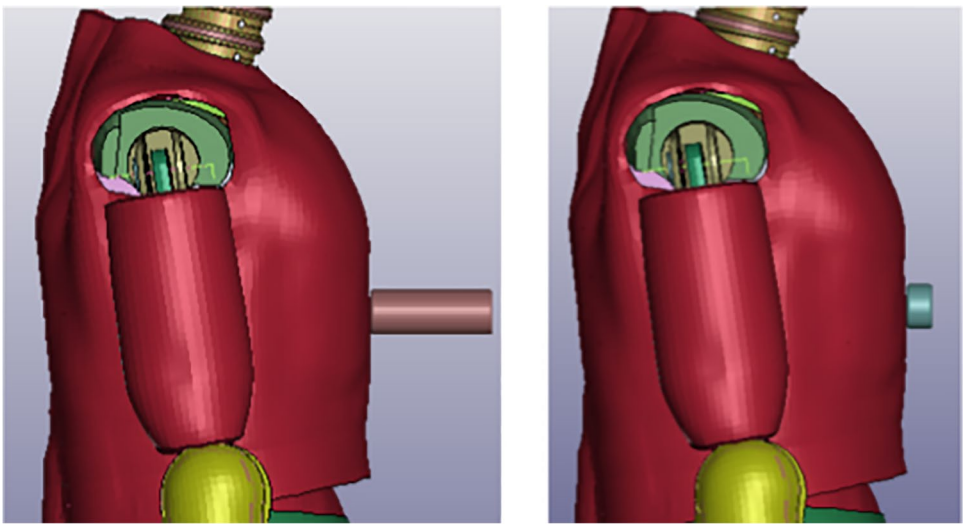

Fig. 14 L5 projectiles impacted the finite element model of the Hybrid III dummy

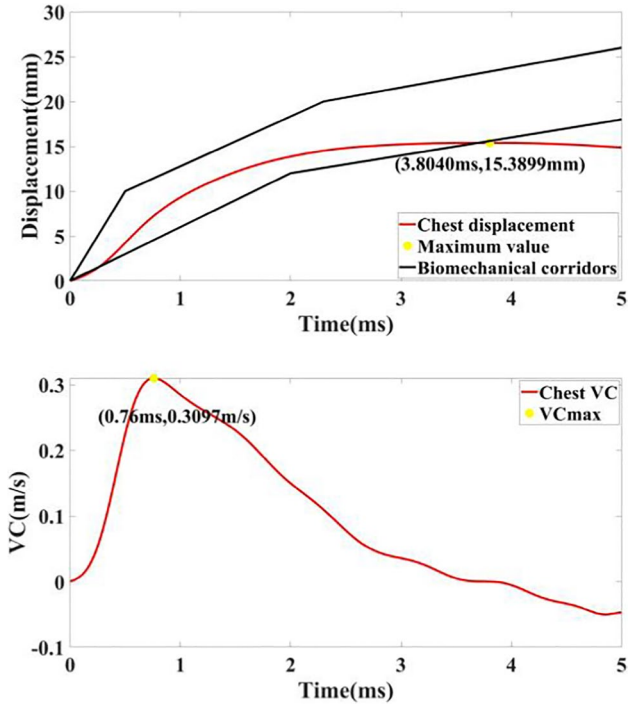

Fig. 15 Curves of thorax displacement and $(VC)_{max}$ of the L5 long projectile impacting dummy model in testing condition 3

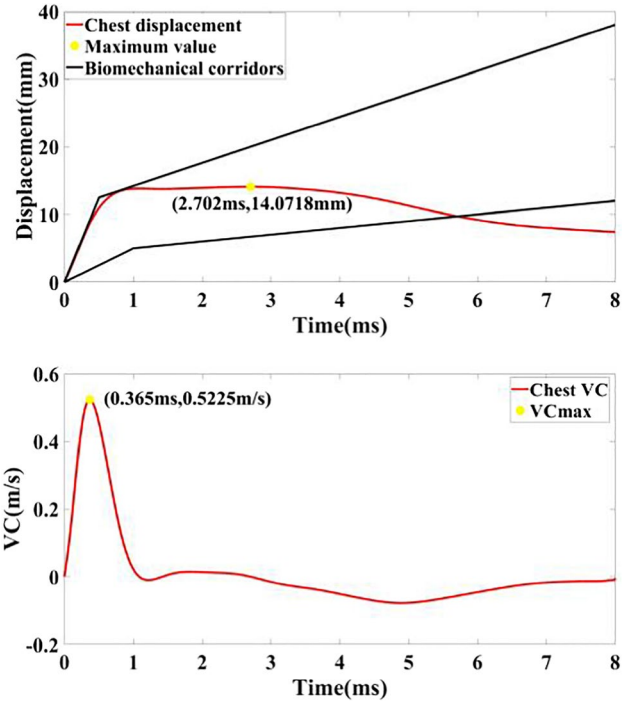

Fig. 17 Curves of thorax displacement and $(VC)_{max}$ of the L5 short projectile impacting dummy model in testing condition 5

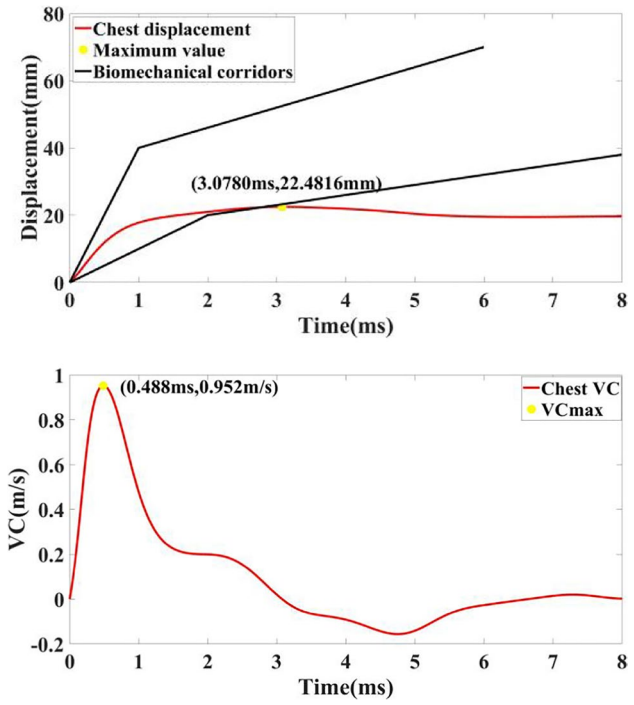

Fig. 16 Curves of thorax displacement and $(VC)_{max}$ of the L5 long projectile impacting dummy model in testing condition 4

projectile when impacting the thorax of the dummy model. The rib displacement data measured by the rib displacement sensor of the Hybrid III dummy is relatively easy and accurate to obtain. We attempted to use the rib displacement data in three testing conditions to build the prediction model. Figure 18 shows the rib displacement data in three testing conditions.

The rib displacement curves in three testing conditions are lower than the lower limit of the corridors, mainly because the skin deformation absorbs most of the kinetic energy when the L5 projectile impacts the thorax (as shown in Fig. 19).

At 1 ms, the skin deformation under three testing conditions has absorbed most of the kinetic energy of the L5 projectiles, so the kinetic energy transferred to the rib has been reduced.

To predict the injury risk of blunt impact on the thorax by kinetic energy projectiles, we attempted to correlate the measured rib displacement with the surface displacement of the cadavers. We tried to connect the measured rib displacement with the surface displacement of the thorax of cadavers in the WSU experiment. We excavated the substitution relationship between the rib displacement and the thoracic surface displacement of the cadavers to indirectly predict the injury risk of the blunt impact of the human thorax.

Thirteen cadavers were used in the WSU experiment. From the anthropometric data of these cadavers, the No.

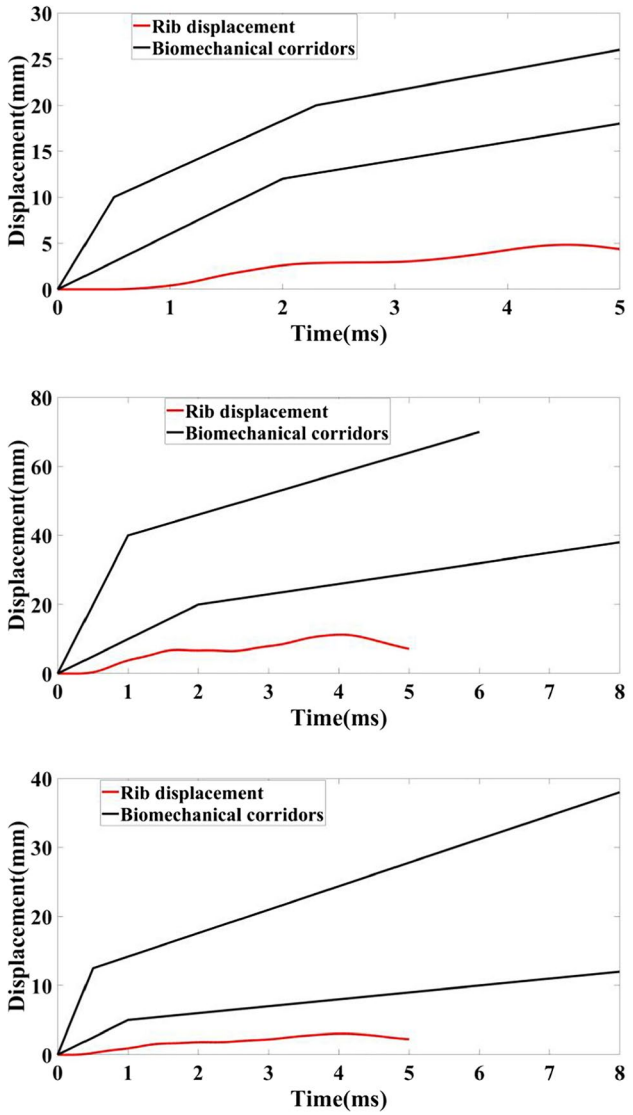

Fig. 18 The rib displacement curves in three testing conditions

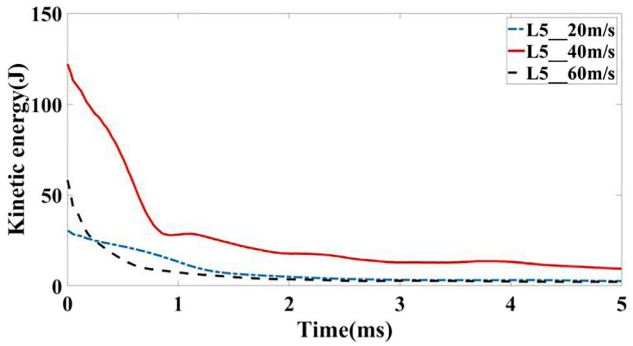

Fig. 19 The kinetic energy of L5 projectiles under three testing condition

Table 7 The measurements of Hybrid III dummy and No. 13 cadaver

	Height/cm	Mass/kg	Chest depth/cm	Chest circumference/cm
Hybrid III dummy	175	79.6	27.3	98.5
No. 13 cadaver	178	82	28	109

Table 8 The fitting index of two displacement curves

Index	R^2	F	P	Constant	Slope
	0.939	1640	1.1e − 66 < 0.001	2.296	3.65

13 cadaver close to the measurement data of the Hybrid III dummy was selected. The measurement data of both are shown in Table 7.

Testing Condition 3

In testing condition 3, since the rib displacement of the dummy model lags behind the surface displacement of the No. 13 cadaver, the starting time point of the rib displacement is 0.5 ms. MATLAB fitted the two displacement curves. The main fitting indicators are shown in Table 8, and the fitting results show a significant linear correlation.

The displacement of the thorax surface of the No. 13 cadaver is Y_A, the rib displacement of the dummy model is X_A, and the linear fitting equation is:

$$Y_A = 3.650X_A + 2.296 \tag{9}$$

The linear correlation coefficient of the two displacement curves is 0.9689, and the fitting figure and $(VC)_{max}$ are shown in Fig. 20.

To test the validity of the fitting results, we carried out an error analysis between the fitting value and the surface displacement of the body's thorax, as shown in Fig. 21. The mean value of the error is $7.4966e-16 \approx 0$, and the sample variance is 2.645.

According to the Kolmogorov–Smirnov test, $P = 0.3975 > 0.05$, so accept the zero hypotheses that curve fitting and the displacement curves of the body's thorax come from the same distribution. To further validate, the Q-Q graph tested its randomness, the random variable of the error term. Kolmogorov–Smirnov was again used to test whether the normalization error has a standard normal distribution, as shown in Fig. 22. Test P value $= 0.8807 > 0.05$, indicating that the normalized error follows the standard normal distribution. Therefore, the linear regression model of Eq. (10) is validated. Its general linear regression model is:

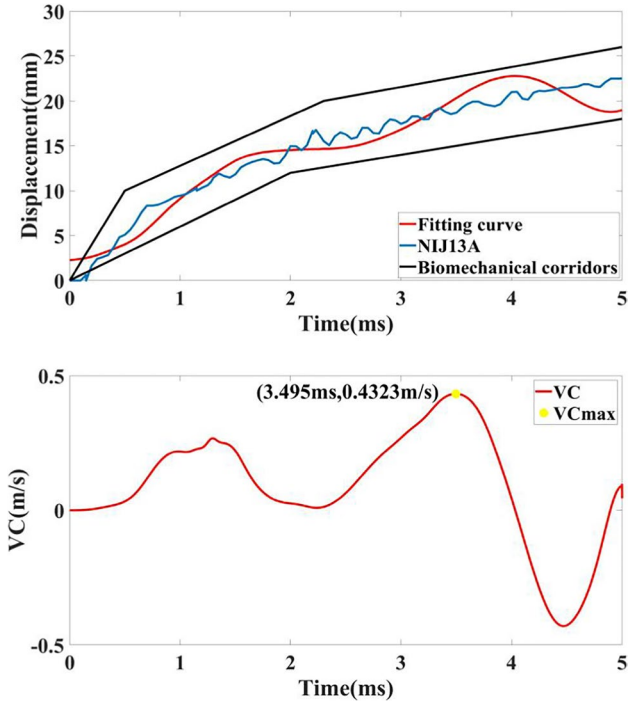

Fig. 20 The fitting figure of displacement and $(VC)_{max}$

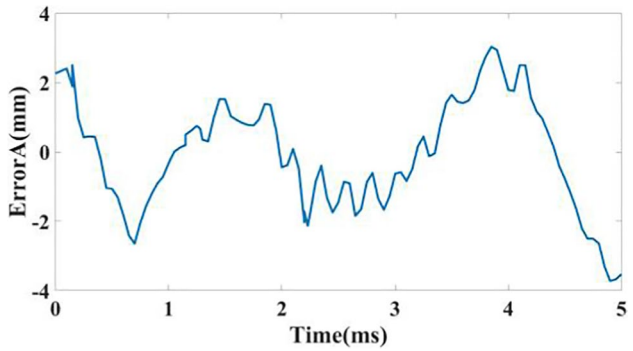

Fig. 21 Error analysis of displacement fitting

$$Y_A = 3.650X_A + 2.296 + \varepsilon \tag{10}$$

where $\varepsilon \sim N(0, 2.645)$.

Testing Condition 4

In testing condition 4, since the rib displacement of the dummy model lags behind the surface displacement of the No. 13 cadaver, the starting time point of the rib displacement is 0.325 ms. MATLAB fitted the two displacement curves. The main fitting indicators are shown in Table 9, and the fitting results show a significant linear correlation.

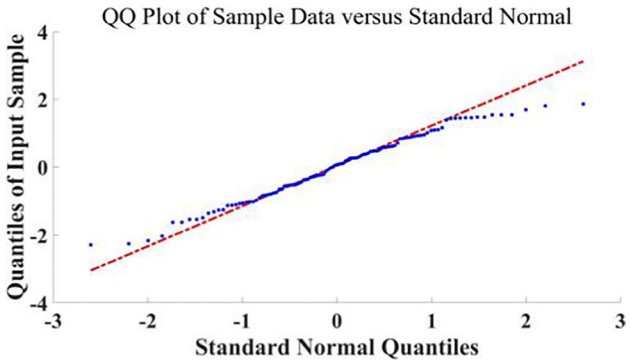

Fig. 22 Q-Q diagram test of random variables with error term

Table 9 The fitting index of two displacement curves

Index	R^2	F	P	Constant	Slope
	0.888	451	9.5e − 66 < 0.001	2.0043	2.5647

The displacement of the thorax surface of the No. 13 cadaver is Y_B, the rib displacement of the dummy model is X_B, and the linear fitting equation is:

$$Y_B = 2.5647X_B + 2.0043 \tag{11}$$

The linear correlation coefficient of the two displacement curves is 0.9422, and the fitting figure and $(VC)_{max}$ are shown in Fig. 23.

To test the validity of the fitting results, we carried out an error analysis between the fitting value and the surface displacement of the body's thorax, as shown in Fig. 24. The mean error is 0.0017≈0, and the sample variance is 12.0147.

According to the Kolmogorov–Smirnov test, $P = 0.4655 > 0.05$, so accept the zero hypotheses that curve fitting and the displacement curves of the body's thorax come from the same distribution. To further validate, the Q-Q graph tested its randomness, the random variable of the error term. Kolmogorov–Smirnov was again used to test whether the normalization error has a standard normal distribution, as shown in Fig. 25. Test P value = 0.6477 > 0.05, indicating that the normalized error follows the standard normal distribution. Therefore, the linear regression model of Eq. (12) is validated. Its general linear regression model is:

$$Y_B = 2.5647X_B + 2.0043 + \varepsilon \tag{12}$$

where $\varepsilon \sim N(0, 12.0147)$.

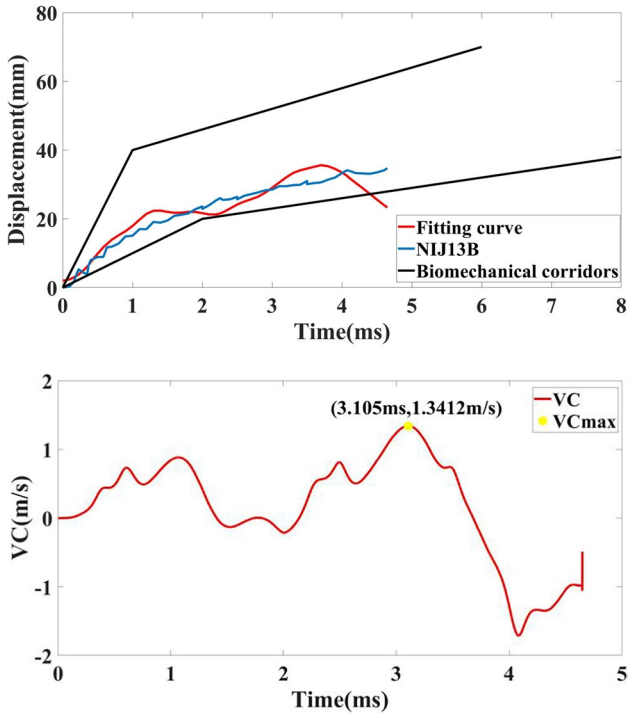

Fig. 23 The fitting figure of displacement and $(VC)_{max}$

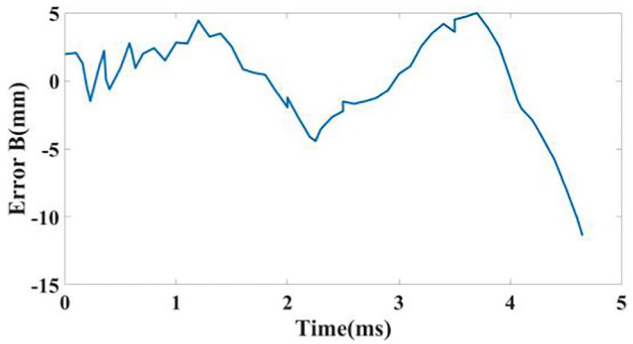

Fig. 24 Error analysis of displacement fitting

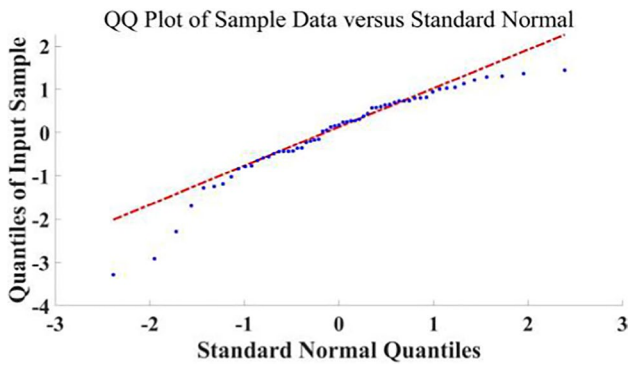

Fig. 25 Q-Q diagram test of random variables with error term

Table 10 The fitting index of two displacement curves

Index	R^2	F	P	Constant	Slope
	0.909	1200	2.54e − 64 < 0.001	1.8985	5.8429

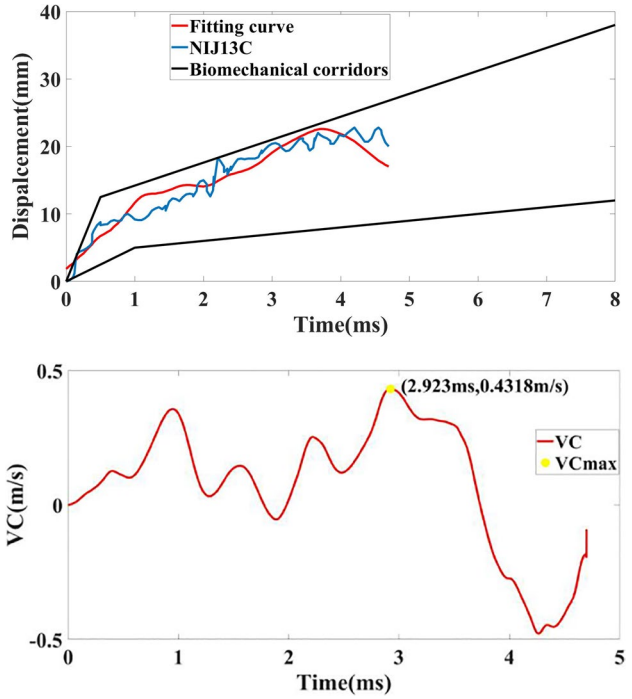

Fig. 26 The fitting figure of displacement and $(VC)_{max}$

Testing Condition 5

In testing condition 5, since the rib displacement of the dummy model lags behind the surface displacement of the No. 13 cadaver, the starting time point of the rib displacement is 0.3 ms. MATLAB fitted the two displacement curves. The main fitting indicators are shown in Table 10, and the fitting results show a significant linear correlation.

The displacement of the thorax surface of the No. 13 cadaver is Y_C, the rib displacement of the dummy model is X_C, and the linear fitting equation is:

$$Y_C = 5.8429X_C + 1.8985 \tag{13}$$

The linear correlation coefficient of the two displacement curves is 0.9535, and the fitting figure is shown in Fig. 26.

To test the validity of the fitting results, we carried out an error analysis between the fitting value and the surface displacement of the body's thorax, as shown in Fig. 27. The mean error is 7.5012e − 05≈0, and the sample variance is 3.2881.

According to the Kolmogorov–Smirnov test, P=0.1725>0.05, so accept the zero hypotheses that curve fitting and the body's thorax surface displacement curves come

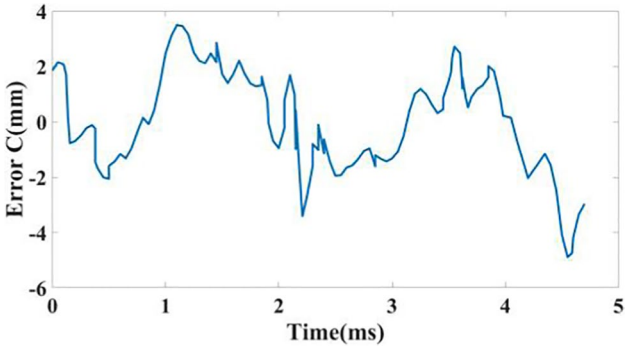

Fig. 27 Error analysis of displacement fitting

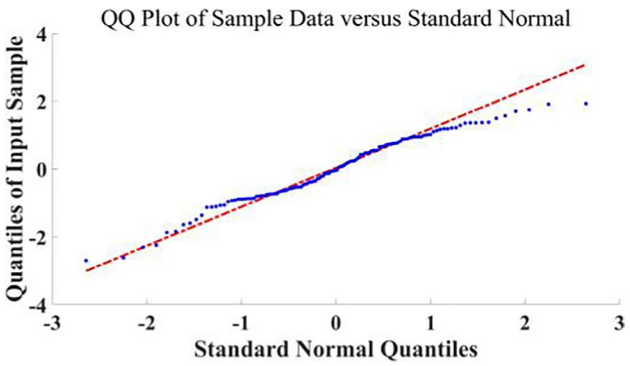

Fig. 28 Q-Q diagram test of random variables with error term

from the same distribution. To further validate, the Q-Q graph tested its randomness, the random variable of the error term. Kolmogorov–Smirnov was again used to test whether the normalization error has a standard normal distribution, as shown in Fig. 28. Test P value = 0.5516 > 0.05, indicating that the normalized error follows the standard normal distribution. Therefore, the linear regression model of Eq. (14) is validated. Its general linear regression model is:

$$Y_C = 5.8429X_C + 1.8985 + \varepsilon \tag{14}$$

where $\varepsilon \sim N(0, 3.2881)$.

To sum up, the fitting curves under the three conditions are in the response corridors, and the linear regression model of each fitting curve has passed the Kolmogorov–Smirnov test. Then, through calculation, the $(VC)_{max}$ of each fitting curve is within the range of viscous response. We verified that these three prediction models are practical and can be used to predict the risk of blunt injury to the human thorax.

Injury Prediction of SIR-X Projectile

To predict the injury risk of the blunt impact of the SIR-X sponge projectile on a human thorax, we simulated the effect of the SIR-X projectile on the dummy thorax at a speed of 60 m/s, as shown in Fig. 29. The rib displacement curve is shown in Fig. 30.

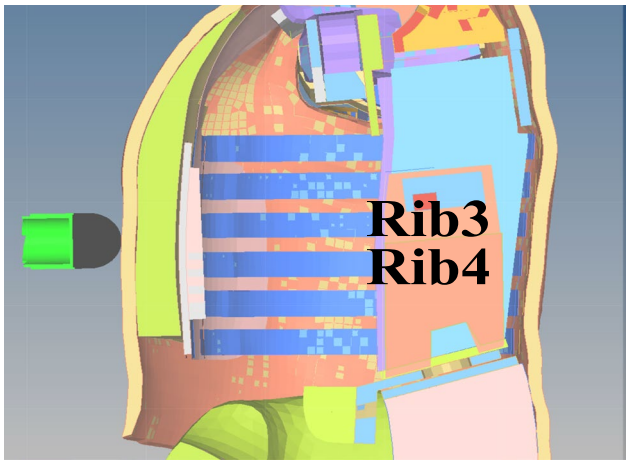

Fig. 29 SIR-X projectiles impacted the finite element model of the Hybrid III dummy

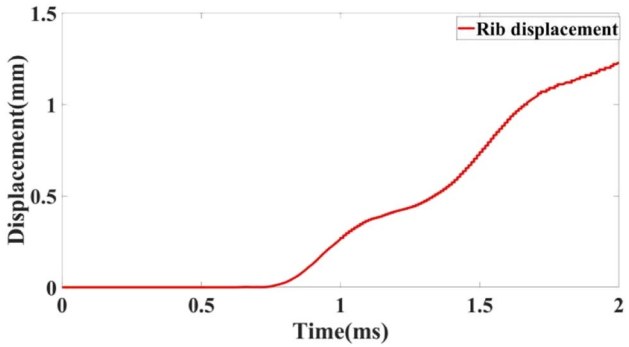

Fig. 30 Curves of thorax displacement of the SIR-X projectile impacting dummy model

Considering that the mass of the SIR-X projectile is close to that of the L5 short projectile, the prediction model of testing condition 5 is used to predict the injury risk of the human thorax. The fitted thoracic surface displacement curve and $(VC)_{max}$ are shown in Fig. 31.

$(VC)_{max} = 0.1606$ m/s is between [0.14,0.65] (Table 10), which verifies the feasibility of the prediction model. The $(VC)_{max}$ of the SIR-X projectile is lower than that of the L5 projectile (Fig. 26), indicating that the kinetic energy projectile of the soft deformable material has a lower risk of injury to the human thorax.

Conclusion

This paper's finite element models of the L5 projectile, SIR-X projectile, and Hybrid III 50th dummy finite element model were constructed and validated by numerical simulation technology. Through simulating the impact on the thorax of the Hybrid III dummy model, the idea of replacing the human

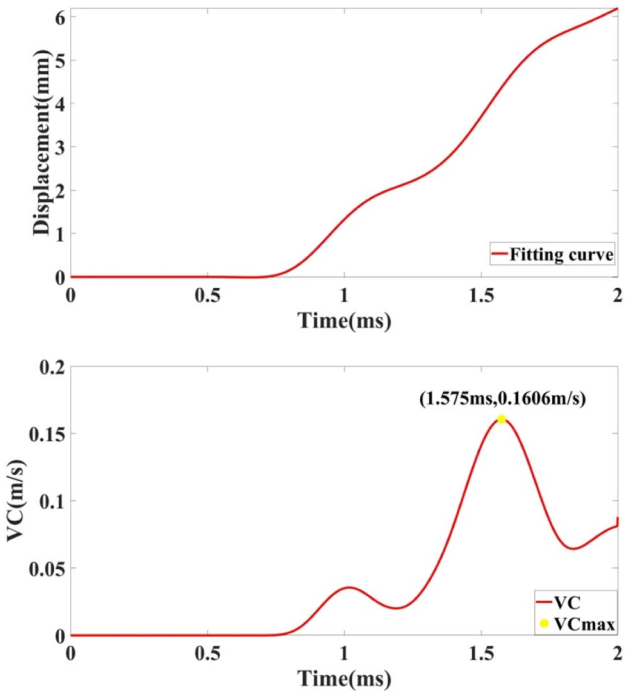

Fig. 31 The fitting figure of displacement and $(VC)_{max}$

body model with the Hybrid III dummy model was proposed. We were considering that in future experiments, the nose of the SIR-X projectile will deform when it impacts the dummy, affecting the high-speed camera to accurately capture the thoracic displacement data at the impact point. Therefore, we attempt to establish a mathematical model to predict the injury risk of blunt impact through multiple simulation tests. Based on the data directly obtained from the rib displacement sensor, we can expect the injury risk of the human thorax through this mathematical model.

The mainstream kinetic energy projectiles are mainly 40-mm caliber soft deformable projectiles. However, the number of prediction models studied in this paper is relatively limited. In the subsequent simulation and experimental tests, the prediction models of various types and different speeds will be covered, which can better provide user decision support in practical applications and minimize the probability of severe injury and death as much as possible.

Author contributions Chaoming Chen wrote the main manuscript text and mainly conductd simulation tests, Fadong Zhao provided the framework of this manuscript, Zongmin Ma mainly carried out data processing and analysis. All authors reviewed the manuscript.

Funding This study was supported by the Science Foundation for Innovative Research Team of the Engineering University of PAP (Project KYTD201905), China.

Declarations

Competing Interests The authors declare no competing interests.

References

1. Sarani B, Hendrix C, Matecki M et al (2019) Wounding patterns based on firearm type in civilian public mass shootings in the United States [J]. J Am Coll Surg 228(3):228–234
2. Kudzinskas A, Callahan A L. Anatomy, thorax[M]//StatPearls [Internet]. StatPearls Publishing, 2020.
3. Kapeles J A, Bir C A. Human effects assessment of 40-mm nonlethal impact munitions [J]. Human Factors and Mechanical Engineering for Defense and Safety (S2509–8004), 2019, 3(1): 1–11.
4. Xiong M, Qin B, Wang S, et al. Experimental impacts of less lethal rubber spheres on a skin-fat-muscle model [J]. Journal of Forensic and Legal Medicine (S1752–928X), 2019, 67: 7–14.
5. Bracq A, Delille R, Maréchal C et al (2019) Rib fractures prediction method for kinetic energy projectile impact: from blunt ballistic experiments on SEBS gel to impact modeling on a human torso FE model [J]. Forensic Sci Int 297:177–183
6. Viano DC, Lau IV (1988) A viscous tolerance criterion for soft tissue injury assessment. J Biomech 21(5):387–399
7. Pavier J, Langlet A, Eches N et al (2015) Experimental study of the coupling parameters influencing the terminal effects of thoracic blunt ballistic impacts [J]. Forensic Sci Int 252:39–51
8. Wu T, Antona-Makoshi J, Alshareef A et al (2020) Investigation of cross-species scaling methods for traumatic brain injury using finite element analysis [J]. J Neurotrauma 37(2):410–422
9. Young LA, Rule GT, Bocchieri RT et al (2015) Biophysical mechanisms of traumatic brain injuries [C]//Seminars in neurology. Thieme Med Publishers 35(01):005–011
10. Prat N, Rongieras F, de Freminville H, et al. Comparison of thoracic wall behavior in large animals and human cadavers submitted to an identical ballistic blunt thoracic trauma [J]. Forensic science international (S0379–0738), 2012, 222(1/2/3): 179–185.
11. Hwang E, Hu J, Chen C et al (2016) Development, evaluation, and sensitivity analysis of parametric finite element whole-body human models in side impacts [J]. Stapp Car Crash J 60:473–508
12. Kalra A. Developing fe human models from medical images[M]// Basic finite element method as applied to injury biomechanics. Academic Press, 2018: 389–415.
13. Meng S. Numerical modeling of impacts at high velocities by a meshfree method smoothed particles hydrodynamics. Application to micro-impacts in soft tissues[D]. Université Bourgogne Franche-Comté, 2021.

14. Valsamos G, Larcher M, Casadei F (2021) Beirut explosion 2020: a case study for a large-scale urban blast simulation [J]. Saf Sci 137:105190
15. Bir, C. A. The evaluation of blunt ballistic impacts of the thorax. Wayne State University, 2000.
16. Century Dynamics. Autodyn introductory training course, 2004.
17. NATO/PFP unclassified. STANREC 4744 ed. 3 (draft) - AEP-99(2021版) ed.A, vol.1 (draft) on thorax injury risk assessment of non-lethal projectiles.
18. Nsiampa N, Robbe C, Papy A (2018) Non-lethal projectile characterisation method: application to 40-mm SIR-X and condor NT901 projectiles [J]. Hum Factors Mech Eng Def Saf 2(1):1–13